Article

On-surface synthesis and characterization of anti-aromatic cyclo[12]carbon and cyclo[20]carbon

Luye Sun[1,3], Wei Zheng[1,3], Faming Kang[1], Wenze Gao[1], Tongde Wang[2], Guohua Gao[2] & Wei Xu [1] ✉

Cyclo[n]carbons have recently attracted significant attention owing to their geometric and electronic structures remaining largely unexplored in the condensed phase. In this work, we focus on two anti-aromatic cyclocarbons, namely C_{12} and C_{20}. By designing two fully halogenated molecular precursors both including 4-numbered rings, we further extend the on-surface retro-Bergman ring-opening reaction, and successfully produce C_{12} and C_{20}. The polyynic structures of C_{12} and C_{20} are unambiguously revealed by bond-resolved atomic force microscopy. More importantly, subtly positioning the C_{20} molecule into an atomic fence formed by Cl clusters allows us to experimentally probe its frontier molecular orbitals, yielding a transport gap of 3.8 eV measured from scanning tunneling spectroscopy. Our work may advance the field by easier synthesis of a series of cyclocarbons via on-surface retro-Bergman ring-opening strategy.

Molecular carbon allotropes, cyclo[n]carbons (C_n) have fascinated a number of experimentalists and theoreticians because of their unique structures and potential applications. Nevertheless, their synthesis in condensed phase is hardly achieved due to the high reactivity, resulting in the geometric and electronic structures of these species remaining largely unexplored[1–15]. On-surface synthesis has demonstrated advantage for the generation of a series of cyclocarbons, for example, C_{18}[16,17], C_{16}[18], C_{14}[19], C_{10}[19] on the NaCl surface, and their geometric structures have been revealed in real space. However, endeavors to synthesize larger cyclocarbons (e.g., C_{20} or C_{24}) have encountered difficulties owing to the unstability of precursor molecules[18]. Meanwhile, it has been extremely challenging to probe the electronic structures of cyclocarbons due to their high mobilities on the NaCl surface.

For smaller anti-aromatic cyclocarbons, e.g., C_{12}, the combination of increased strain and reduced stability further complicates their synthesis. Specifically, theory predicted that the bond angle alternation drastically changes from C_{16} (BAA = 0.03°) to C_{12} (BAA = 36.9°)[11]. On the other hand, for larger ones (e.g., $n > 18$), monocyclic, bicyclic or polycyclic isomers were predicted by theory or identified experimentally in the gas phase[20–22]. Especially, the carbon cluster ($n = 20$) is considered to be the transition point from monocyclic to bicyclic/polycyclic structures[23–26]. Thus, synthesizing and characterizing the geometric and electronic structures of C_{12} and C_{20} in the condensed phase are of particular interest.

Considering the anti-aromatic nature of these two cyclocarbons, herein, we designed and synthesized two molecular precursors both including 4-numbered rings, i.e., a fully halogenated biphenylene (1,4,5,8-tetraiodo-2,3,6,7-tetrabromobiphenylene, $C_{12}Br_4I_4$) and dibenzo[b,h]biphenylene (perchlorodibenzo[b,h]biphenylene, $C_{20}Cl_{12}$). Through scanning tunneling microscopy (STM) tip-induced dehalogenation and accompanied retro-Bergman ring-opening reactions, C_{12} was successfully generated on the surface (Fig. 1a). Such a strategy is also very recently followed by Gross and Anderson's groups to produce C_{13}[27]. Moreover, through on-surface transformation from hexagon-tetragon (6–4) carbon rings to pentalene moiety (5–5) and followed by dehalogenation and more complicated ring-opening reactions, C_{20} was also achieved (Fig. 1b).

[1]Interdisciplinary Materials Research Center, School of Materials Science and Engineering, Tongji University, Shanghai 201804, People's Republic of China. [2]Shanghai Key Laboratory of Special Artificial Microstructure Materials and Technology, School of Physics Science and Engineering, Tongji University, Shanghai 200092, People's Republic of China. [3]These authors contributed equally: Luye Sun, Wei Zheng. ✉e-mail: xuwei@tongji.edu.cn
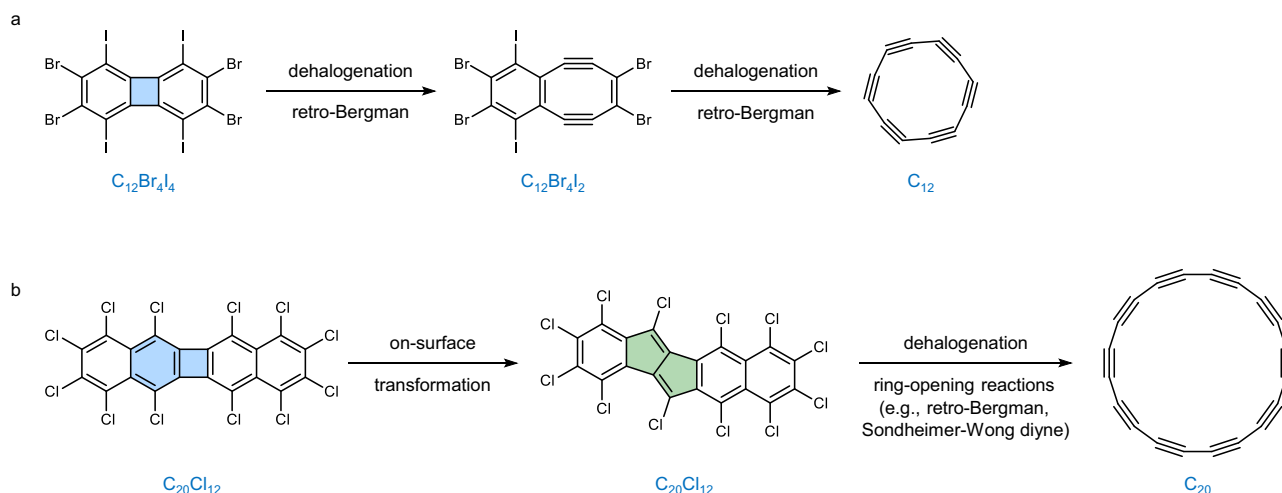
Fig. 1 | Reaction scheme toward the formation of cyclo[12]carbon and cyclo[20] carbon. a Reaction scheme for the formation of C_{12} (tetragon carbon ring of the precursor colored in blue). **b** Reaction scheme for the formation of C_{20} through transformation from hexagon-tetragon (6–4) carbon rings (colored in blue) to pentalene moiety (5–5) (colored in green) and followed by dehalogenation and ring-opening reactions.

Results

On-surface synthesis of cyclo[12]carbon

For anti-aromatic cyclo[12]carbon, two polyynic structures with D_{6h} and C_{6h} symmetries (Supplementary Fig. 1a, b) are considered. Based on modern theories[11,12], it is predicted that the lowest energy geometry of C_{12} is C_{6h} polyynic structure (Supplementary Fig. 1b), featuring a bond length alternation (BLA = 0.13 Å), and a bond angle alternation (BAA = 36.9°) (Supplementary Fig. 2).

To generate C_{12}, $C_{12}Br_4I_4$ molecules were introduced on the cold sample held at ~6 K. All molecules were studied on a 1-3 ML NaCl/Au(111) surface at 4.7 K. High-resolution atomic force microscopy (AFM) image acquired with CO-terminated tip revealed both the carbon skeleton (6-4-6-membered ring) and eight halogen atoms of the $C_{12}Br_4I_4$ molecule (Fig. 2a $_{II}$), which were also clearly shown in the AFM simulation and Laplace-filtered AFM images (Fig. 2a $_{III}$ and a $_{IV}$). To trigger dehalogenation reactions, the tip was initially positioned on a single $C_{12}Br_4I_4$ molecule, and retracted by ~3 Å from a setpoint (typically I = 0.4 pA, V = 0.3 V), after that, ~3 V pulse was applied on the molecule with currents on the order of a few pA. Normally, one or two iodine atoms were first removed, leading to the formation of $C_{12}Br_4I_3$ (Supplementary Fig. 3a) or $C_{12}Br_4I_2$ (Fig. 2b) intermediates. The AFM image (Fig. 2b $_{II}$) revealed that the first-step retro-Bergman ring-opening reaction has already occurred in a $C_{12}Br_4I_2$ molecule, leading to the formation of an 8-membered ring (also refer to Fig. 1a). In addition, two characteristic bright features corresponding to the carbon-carbon triple bonds were observed (also see our calculations in Supplementary Fig. 4a and the simulation in Fig. 2b $_{III}$), which are more clearly shown in the Laplace-filtered AFM image (Fig. 2b $_{IV}$). Further dehalogenation and accompanied second-step retro-Bergman reaction led to the formation of $C_{12}Br_3$ intermediate (Fig. 2c $_{II}$), which was imaged as a larger carbon ring and three Br atoms attached, where four characteristic bright features corresponding to the triple bonds could be distinguished, as also shown in the AFM simulation and Laplace-filtered AFM image (Fig. 2c $_{III}$ and c $_{IV}$). The bond lengths calculation of such a 12-membered ring was shown in Supplementary Fig. 4b. Other observed intermediates during pulses were shown in Supplementary Fig. 3b–d.

Subsequent voltage pulses (~3-3.5 V) could induce complete dehalogenation of intermediates (e.g., Fig. 2c and Supplementary Fig. 3b–d), resulting in the formation of the final products as shown in the AFM images (Fig. 2d and Supplementary Fig. 5). AFM images show a single carbon ring with no halogen atoms attached, which can be unambiguously recognized as a C_{12}. More importantly, six pronounced characteristic bright features are clearly distinguished in the AFM images, which were assigned to six triple bonds of C_{12}, that means, the anti-aromatic C_{12} also adopts an energetically favorable polyynic structure as the ground state, similar to the case of C_{16}[18]. The assignment of six triple bonds is also supported by AFM simulation (Fig. 2d $_{III}$). It is noticeable that C_{12} possesses a moderate bond length alternation (BLA $_{C12}$ = 0.13 Å) (Supplementary Fig. 2) among already generated cyclocarbons on the surface (i.e., BLA $_{C18}$ = 0.12 Å, BLA $_{C16}$ = 0.15 Å, BLA $_{C14}$ = 0.04 Å, BLA $_{C10}$ = 0 Å, calculated at the ωB97XD/def2-TZVP level[11]). In the close tip-sample height (Supplementary Fig. 6), bright lines appear between triple bonds, which should originate from the tip-tilting effect[28]. The DFT calculations of C_{12} on the NaCl surface at different sites show near-planar adsorption configurations (Supplementary Fig. 7). Our experimental results verify the polyynic structure of C_{12} predicted by modern theories, while, the D_{6h} or C_{6h} symmetries cannot be distinguished in AFM images[17].

During our experiments, we realized that the thickness of NaCl is a rather important point for the successful generation of C_{12}. We have respectively tried different thickness of NaCl, e.g., 1 ML, 2 ML, 3 ML, and found out that the yield is highest on the 1 ML NaCl surface. We have attempted 15 precursors and successfully generated 7 individual C_{12} on the 1 ML NaCl surface with a yield of about 46.7%. We have attempted 8 precursors and successfully generated 1 individual C_{12} on the 2 ML NaCl surface with a yield of 12.5%. We have attempted 12 precursors and successfully generated 1 individual C_{12} on the 3 ML NaCl surface with a yield of about 8.3%. The main reason for the unsuccessful attempts is the disturbance of intermediates during imaging on the NaCl surfaces. At given STM setpoints the tip is closer to the molecule with increasing NaCl thickness, and thus more likely displaces the molecule during STM imaging.

On-surface synthesis of cyclo[20]carbon

To generate larger anti-aromatic cyclocarbon, e.g., C_{20}, $C_{20}Cl_{12}$ molecules were introduced on the cold sample held at ~6 K. All molecules were studied on a 1 ML NaCl/Au(111) surface at 4.7 K. AFM and STM images (Fig. 3a $_{II}$ and a $_{III}$, also Supplementary Fig. 8) revealed its nonplanar adsorption configuration on the NaCl surface due to steric hindrance (refer to the model in Fig. 3a $_{IV}$)[29]. To induced dehalogenation reactions, the tip was initially positioned on a single $C_{20}Cl_{12}$ molecule, and retracted by ~4 Å from a setpoint (typically I = 5 pA, V = 0.3 V), after that, ~4 V pulse was applied on the molecule with
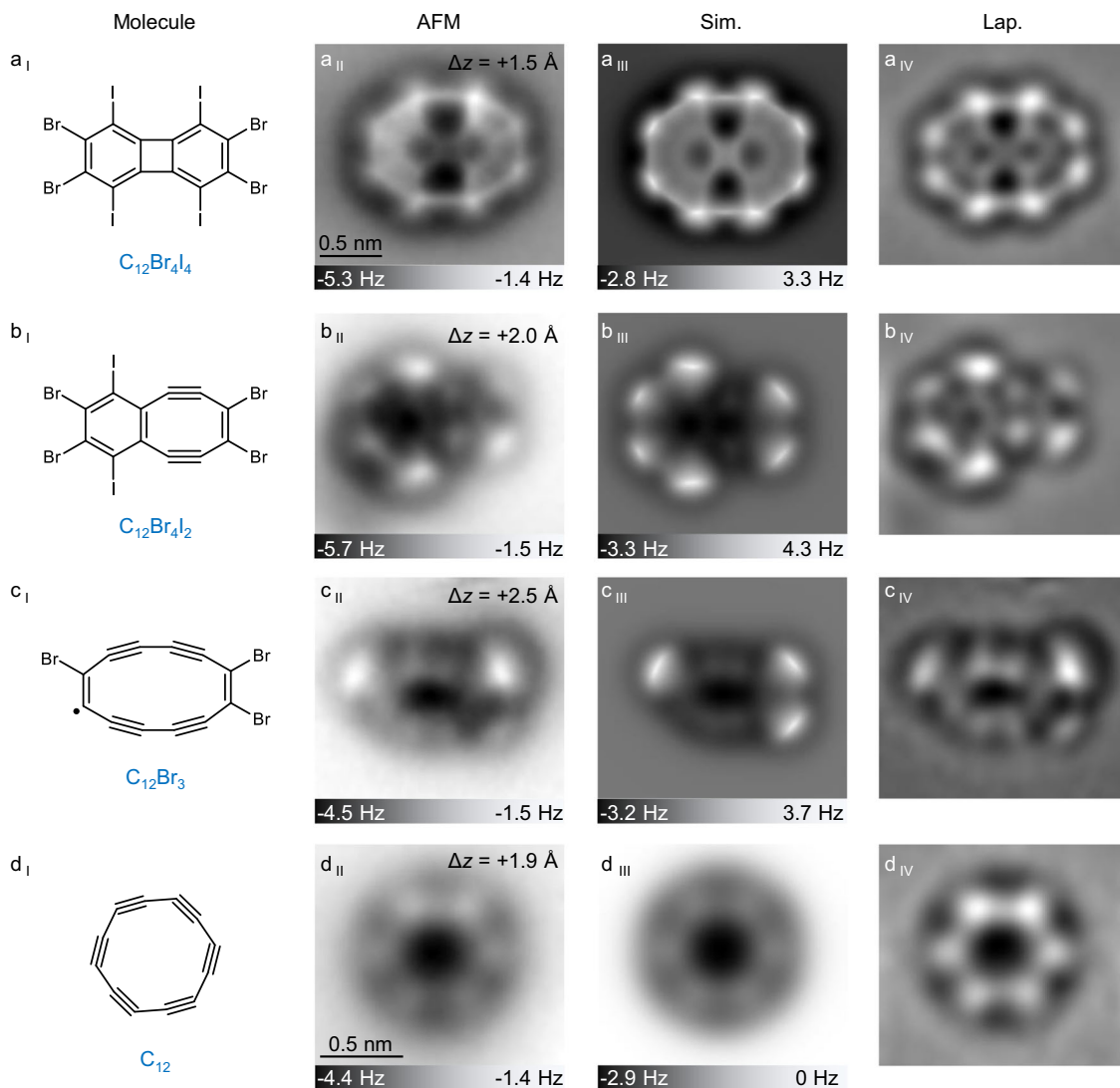
Fig. 2 | On-surface generated precursor, intermediates, and product (C_{12}).
a I–**a** IV, **b** I–**b** IV, **c** I–**c** IV, **d** I–**d** IV Molecular structures, AFM images, AFM simulations, and Laplace-filtered AFM images of precursor, typical intermediates, and product. AFM simulations are based on gas-phase DFT-calculated geometries. The scale bar in (**a** II) applies to all images of precursor and intermediates, and the scale bar in (**d** II) applies to all images of product. All molecules in Fig. 2 were studied on a 3 monolayer (ML) NaCl/Au(111) surface. Reference set point of Δz for **a** II to **d** II: $I = 0.4$ pA, $V = 0.3$ V.

currents on the order of a few pA. Subsequent high-resolution AFM images (Fig. 3b and also Supplementary Fig. 9) showed that the typically observed intermediates became more planar as a result of dehalogenation at different sites. In addition, it is noted that the carbon skeleton of each observed intermediate molecule has undergone the transformation from a 6–4 configuration to pentalene moiety (5-5) accompanied with dehalogenation (as shown in Fig. 1b), which was also observed in other on-surface reaction systems[30] and gas-phase experiments[31].

Additional pulses (~ 4 V) can induce dehalogenation and occurrence of different kinds of ring-opening reactions, e.g., retro-Bergman[19,32–34], formation of Sondheimer-Wong diyne[35,36]. Figure 3c shows the generation of a $C_{20}Cl_2$ intermediate consisting of a 10-membered ring (colored in blue) via a retro-Bergman reaction (the calculated BLAs within this 10-membered ring are shown in Supplementary Fig. 10). More interestingly, Fig. 3d shows the generation of another $C_{20}Cl_2$ intermediate consisting of a newly formed 8-membered ring, indicating the pentalene moiety has changed (additional AFM images in Supplementary Fig. 11). Such a reaction is understood to be the formation of Sondheimer-Wong diyne[36] (the

reaction scheme is shown in Supplementary Fig. 12 together with the calculated BLAs within this 8-membered and 10-membered rings).

Furthermore, intermediates with larger odd-membered carbon rings were also observed as shown in Fig. 3e, f. For example, a 9-membered ring was formed within the $C_{20}Cl_4$ intermediate (Fig. 3e), in which two characteristic bright features assigned to triple bonds were revealed (see calculations on BLAs in Supplementary Fig. 13a). An even larger 13-membered ring was also observed within another $C_{20}Cl_2$ intermediate (Fig. 3f), in which both characteristic bright features (for triple bonds) and uniform line features (for cumulene) were observed in this peculiar ring (see calculations on BLAs in Supplementary Fig. 13b, additional AFM images in Supplementary Fig. 14). Figure 3g shows another $C_{20}Cl_2$ intermediate with a 16-membered ring, which could arise from direct ring-opening of an 8- and a 10-membered ring, or a 5- and a 13-memebered ring. Seven characteristic bright features in AFM images point out the location of triple bonds (see calculations on BLAs in Supplementary Fig. 15), in agreement with the results of C_{16} intermediate ($C_{18}O_2$)[18]. In our experiments, the tip-induced dehalogenation could be related to anionic charge states of molecules or an applied electric field[34,37,38]. In addition, inelastic electron tunnelling
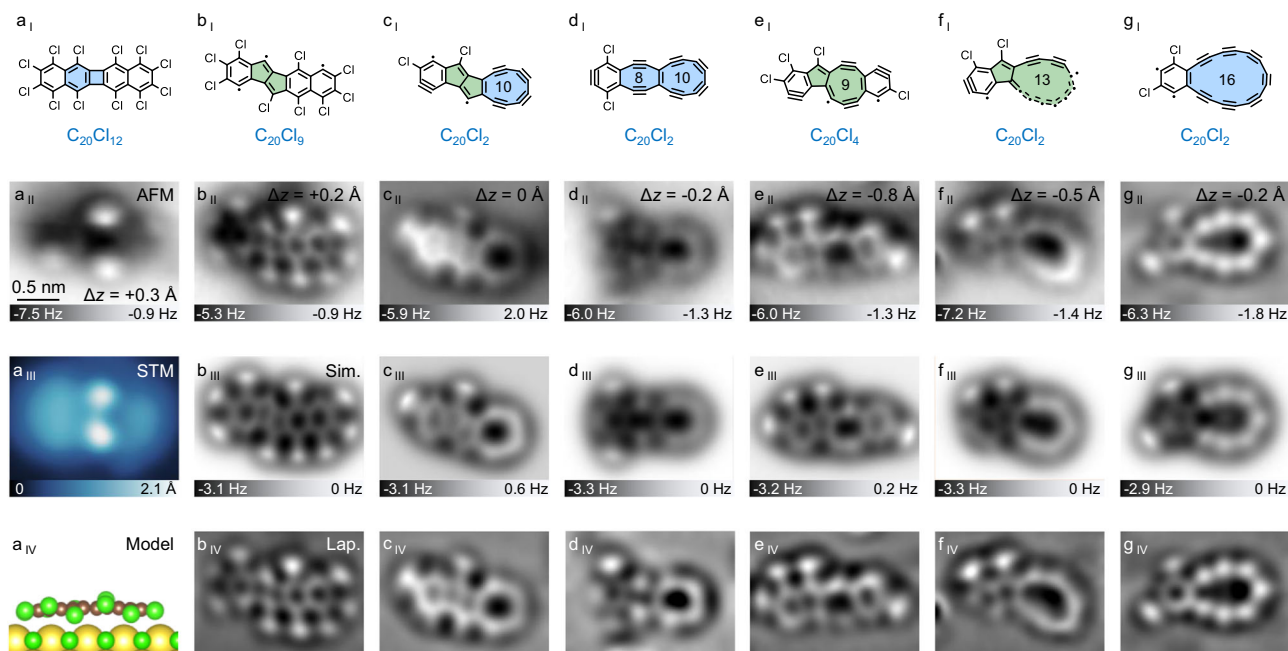
Fig. 3 | Precursor and typical intermediates consisting of larger even- and odd-membered rings. a_I–a_{IV} $C_{20}Cl_{12}$. b_I–b_{IV} $C_{20}Cl_9$. c_I–c_{IV} $C_{20}Cl_2$ with a 10-membered ring. d_I–d_{IV} $C_{20}Cl_2$ with 8- and 10-membered rings. e_I–e_{IV} $C_{20}Cl_4$ with a 9-membered ring. f_I–f_{IV} $C_{20}Cl_2$ with a 13-membered ring. g_I–g_{IV} $C_{20}Cl_2$ with a 16-membered ring. Structures (a_I–g_I), AFM images (a_{II}–g_{II}), AFM simulations (b_{III}–g_{III}), Laplace-filtered AFM images are shown (b_{IV}–g_{IV}). AFM simulations are based on gas-phase DFT-calculated geometries. The scale bar in (a_{II}) applies to all images. Reference set point of Δz for a_{II} to g_{II}: $I = 5$ pA, $V = 0.3$ V.

may also help to trigger dehalogenative reactions[16]. With such voltage pulses, skeletal rearrangements can either be triggered, too, or happen spontaneously as a consequence of the dehalogenation[34].

Subsequent voltage pulses could induce complete dehalogenation of intermediates, resulting in the formation of the final product as shown in the STM and AFM images (Fig. 4a). STM image (Fig. 4a_I) shows a donut shape without much orbital information at a lower bias voltage ($V = 0.3$ V). AFM images (Fig. 4a_{II} and a_{IV}) clearly show a single carbon ring with no halogen atoms attached, which can be unambiguously recognized as a C_{20}. We attempted 27 precursors and generated 5 individual C_{20} molecules on the 1 ML NaCl surface with a yield of about 18.5 %. In the unsuccessful attempts, we frequently found the edge benzoid rings opened as shown in Supplementary Fig. 16. More importantly, ten pronounced characteristic bright features are clearly distinguished in the AFM images, which are assigned to ten triple bonds of C_{20}. Based on the calculations (Supplementary Fig. 17), we verify that the anti-aromatic C_{20} adopts an energetically favorable D_{10h} polyynic structure (Supplementary Fig. 1c) as the ground state, and features a BLA of 0.14 Å, while, D_{10h} or C_{10h} symmetry cannot be distinguished in AFM images. The assignment of ten triple bonds is also supported by AFM simulations (Fig. 4a_{III}). The DFT calculations of a C_{20} on the NaCl surface at different sites show near-planar adsorption configurations (Supplementary Fig. 18).

Electronic characterizations of cyclo[20]carbon

From calculated molecular orbitals of C_{20} (Fig. 4b and Supplementary Fig. 19), it is seen that C_{20} exhibits a doubly anti-aromatic configuration. It has been difficult to measure the electronic states of cyclocarbons due to the high mobility on the NaCl surface. We succeeded in manipulating a C_{20} molecule trapped into an atomic fence formed by eliminated Cl atoms (Supplementary Fig. 20), thus allowing to probe its electronic states by applying relatively larger bias voltages. As shown in Fig. 4c, we have successfully measured the differential conductance as a function of voltage, dI/dV, of a C_{20}. Two peaks show up at $V = -2.25$ V and $V = 1.55$ V, which corresponds to the positive ion resonance (PIR) and the negative ion resonance (NIR)[39], respectively. The

dI/dV spectrum gives a transport gap about 3.8 eV for C_{20}. For PIR, ten characteristic lobes can be seen from STM images (Fig. 4e_I and e_{II}). From the calculations, it is seen that HOMO (in-plane) and HOMO-1 (out-of-plane) orbitals are nearly energetically degenerated, we deduce that the PIR state results from the superposition of HOMO and HOMO-1 orbitals (Fig. 4b), in which ten lobes are located over every triple bond of C_{20}. Meanwhile, ten characteristic lobes are also visualized at NIR state (Fig. 4d_I, d_{II}, f_I, and f_{II}), which should result from the superposition of nearly degenerated LUMO (out-of-plane) and LUMO + 1 (in-plane) orbitals (Fig. 4b), in which ten lobes are located over every single bond. The superimposed structures of C_{20} (Fig. 4e_{II} and f_{II}) determined from theoretical calculations exhibited a slight rotation (~ 8°) compared to the experimental AFM image (the inset of Fig. 4c), and such a rotation might be induced during STM imaging. It is considered that the peaks at the PIR and NIR dominantly relate to the out-of-plane orbitals, that is, HOMO-1 and LUMO, respectively[27]. In addition, due to the energy broadening of the ionic resonances on NaCl (~ 0.3 V)[39], nearly degenerated HOMO/HOMO-1 and LUMO/ LUMO + 1 could not be resolved as separate peaks in dI/dV spectrum.

In conclusion, we have successfully generated two anti-aromatic cyclocarbons, i.e., C_{12} and C_{20}, by atom manipulation and induced ring-opening reactions on the NaCl/Au(111) surface at 4.7 K. The polyynic structure of C_{12} and C_{20} was revealed by bond-resolved AFM imaging, in agreement with theoretical predictions. More importantly, manipulating C_{20} next to Cl clusters to hinder its diffusion makes it possible to probe the electronic structures of C_{20}. We believe such an on-surface synthesis strategy could be further extended to the generation and characterization of other larger cyclocarbons.

Methods

Experimental details for STM and AFM measurements

STM and AFM measurements were carried out in a commercial (Createc) low-temperature system operated at 4.7 K with base pressure better than 1×10^{-10} mbar. Single crystalline Au(111) surface was cleaned by several sputtering and annealing cycles. The NaCl films were obtained by thermally evaporating NaCl crystals onto a clean Au(111)
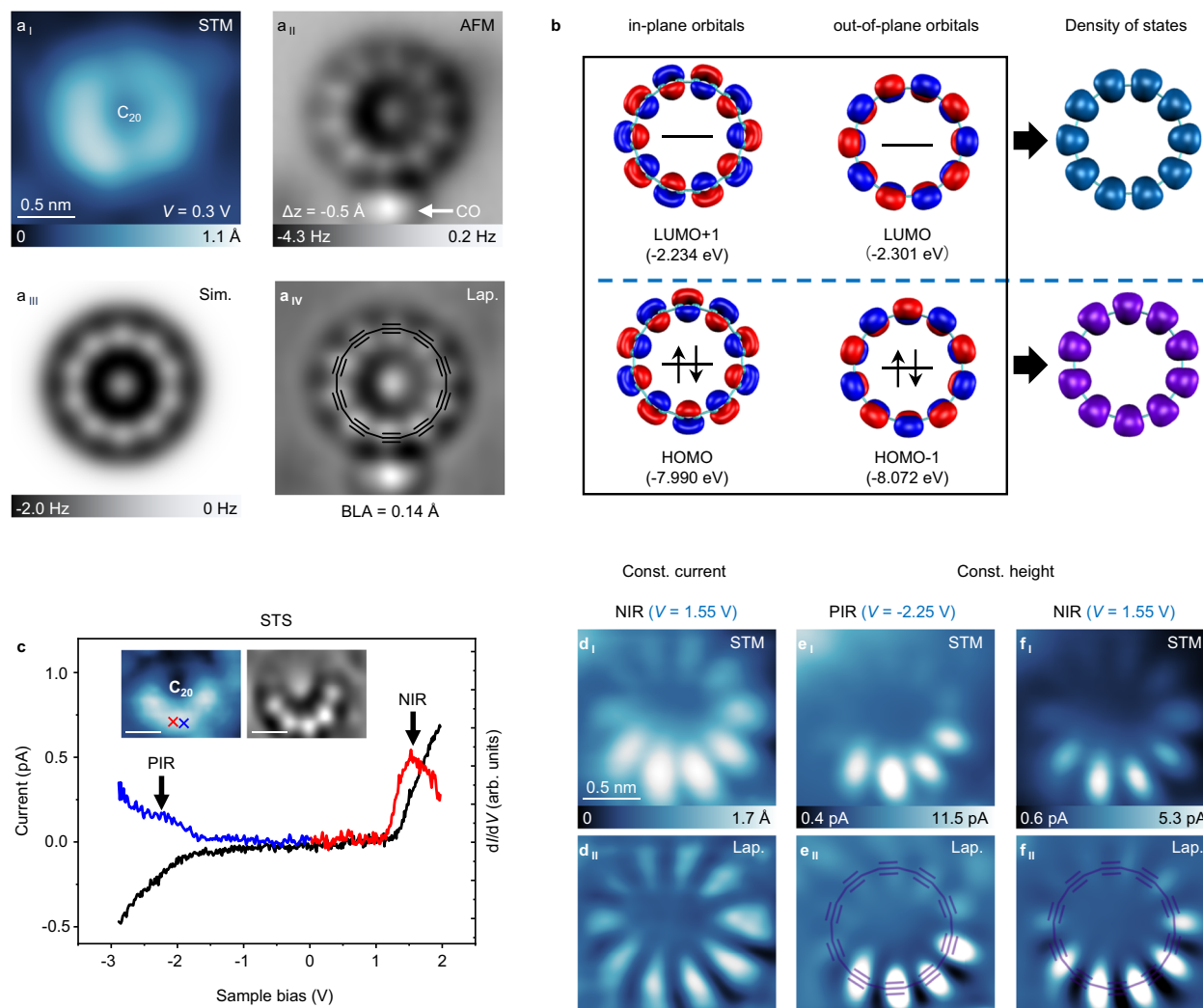
Fig. 4 | The geometric and electronic characterizations of C$_{20}$. a$_I$–a$_{IV}$ STM image, AFM image, AFM simulation, and Laplace-filtered AFM image of a C$_{20}$. STM set points: $I = 5$ pA, $V = 0.3$ V. Reference set point of Δz: $I = 5$ pA, $V = 0.3$ V. **b** Calculated frontier orbitals of C$_{20}$ and superposition of orbital densities of the nearly energetically degenerated orbitals. Calculations were conducted at the ωB97XD/def2-TZVP level. **(c)** Scanning tunneling spectroscopy (STS) of C$_{20}$ conducted on NaCl. The differential conductance (dI/dV) signal shows two peaks that can be attributed to the PIR and NIR states. Inset: STM ($I = 5$ pA, $V = 0.3$ V, 0 to 1.6 Å) and AFM ($\Delta z = -0.6$ Å, reference set point: $I = 5$ pA, $V = 0.3$ V, -3.4 Hz to -0.2 Hz)

images of a C$_{20}$. Scale bar: 0.5 nm. STM images (**d$_I$–f$_I$**) and Laplace-filtered STM images (**d$_{II}$–f$_{II}$**) of C$_{20}$ obtained with a CO-tip. (**d$_I$–d$_{II}$**) NIR, constant current mode; (**e$_I$–e$_{II}$**) PIR, constant height mode ($\Delta z = 0$ Å, reference set point: $I = 5$ pA, $V = -2.25$ V); (**f$_I$ and f$_{II}$**) NIR, constant height mode ($\Delta z = 0$ Å, reference set point: $I = 5$ pA, $V = 1.55$ V). The dI/dV spectrum sweeping from zero to negative bias (blue line) was conducted on the triple bond of C$_{20}$ (blue cross in Fig. 4c), and the dI/dV spectrum sweeping from zero to positive bias (red line) was conducted on the single bond of C$_{20}$ (red cross in Fig. 4c).

surface at room temperature, resulting in islands of one and two monolayer (ML) thickness. After annealing the sample to a temperature of about 373 K, large-area three ML NaCl surface was obtained. The precursor molecule 1,4,5,8-tetraiodo-2,3,6,7-tetrabromobiphenylene (C$_{12}$Br$_4$I$_4$) was synthesized as detailed below using procedures in ref. 40. The precursor molecule perchlorodibenzo[b,h]biphenylene (C$_{20}$Cl$_{12}$) was synthesized as detailed below. C$_{12}$Br$_4$I$_4$ and C$_{20}$Cl$_{12}$ molecules were separately deposited on a cold NaCl/Au(111) surface by thermal sublimation from a molecular evaporator. CO molecules for tip modification[41] were dosed onto the cold sample via a leak valve. We used a qPlus sensor[42] with a resonance frequency $f_0 = 29.49$ kHz, quality factor $Q \approx 45,000$ and a spring constant $k \approx 1800$ N/m operated in frequency-modulation mode[43]. The bias voltage V was applied to the sample with respect to the tip. AFM images were acquired in constant-height mode at $V = 0$ V and an oscillation amplitude of $A = 1$ Å. The tip-height offsets Δz for constant-height AFM images are defined as the offset in tip-sample distance

relative to the STM set point at the NaCl surface. The positive (negative) values of Δz correspond to the tip-sample distance increased (decreased) with respect to a STM set point. With increasing thickness of NaCl, the tip-sample distance decreased at given STM set-point conditions, which normally leads to larger tip-height offsets for constant-height AFM images (see AFM images of C$_{12}$, C$_{20}$ and intermediates on 1-3 ML NaCl surfaces in Supplementary Fig. 21).

Solution synthesis of 1,4,5,8-tetraiodo-2,3,6,7-tetrabromobiphenylene (C$_{12}$Br$_4$I$_4$)

1,4-Bis(trimethylsilyl)-2,3,5,6-tetrabromobenzene: 1,2,4,5-Tetrabromobenzene (10.0 g, 25.4 mmol) and trimethylsilyl chloride (7 mL, 106 mmol) were suspended in anhydrous THF (150 mL) in a flame-dried 500 mL Schlenk flask and cooled to $-78\,^{\circ}$C. Subsequently, a solution of LDA (2 M, 28 mL) was added to this suspension in the course of 30 min. The resulting solution was warmed up to room temperature overnight, quenched with 1 N HCl solution and extracted

with CH_2Cl_2. The combined organic fractions were dried over $MgSO_4$. After filtration and evaporation of the solvent, the residue was subjected to repeated column chromatography (silica, hexane). 1,4-Bis (trimethylsilyl)-2,3,5,6-tetrabromobenzene was obtained as a colorless liquid. (7.0 g, 70 %). ^{1}H NMR ($CDCl_3$, 400 MHz, δ): 0.60 (s).

2,3,6,7-Tetrabromo-1,4,5,8-tetra(trimethylsilyl)biphenylene: To a solution of 1,4-Bis(trimethylsilyl)-2,3,5,6-tetrabromobenzene (5.0 g, 9.29 mmol) in anhydrous THF (40 mL) at −78 °C under argon, nBuLi (5.8 mL, 9.29 mmol, 1.6 M in hexane) was added over one hour. After warming to room temperature overnight, the reaction mixture was quenched with 1 N aqueous HCl solution, extracted with CH_2Cl_2, the combined organic phases were dried over $MgSO_4$ and filtered. The solvents were evaporated *in vacuo* and the residue was subjected to column chromatography (silica, hexane/CH_2Cl_2 8:1), followed by precipitation from MeOH to give 2,3,6,7-Tetrabromo-1,4,5,8-tetra (trimethylsilyl)biphenylene (0.8 g, 10%) as a yellow solid. ^{1}H NMR ($CDCl_3$, 400 MHz, δ): 0.40 (s).

1,4,5,8-tetraiodo-2,3,6,7-tetrabromobiphenylene ($C_{12}Br_4I_4$): In the absence of light a 1 M iodine monochloride solution in CH_2Cl_2 (7.93 mL, 7.93 mmol) was added dropwise over 15 min to 2,3,6,7-Tetrabromo-1,4,5,8-tetra(trimethylsilyl)biphenylene (300 mg, 0.40 mmol) in anhydrous CH_2Cl_2 (20 mL) at 0 °C under argon. After warming to room temperature overnight, the reaction was quenched by the addition of an aqueous Na_2SO_3 solution. The precipitate was filtered and extensively washed with water, MeOH, CH_2Cl_2 and THF, yielding 1,4,5,8-tetraiodo-2,3,6,7-tetrabromobiphenylene as a hardly soluble light yellow solid (190 mg, 50%). The compound was used without further purification.

Solution synthesis of perchlorodibenzo[*b,h*]biphenylene ($C_{20}Cl_{12}$)

The perchlorodibenzo[*b,h*]biphenylene was obtained in two steps: the synthesis of dibenzo[*b,h*]biphenylene ($C_{20}H_{12}$) followed by ref. 44. Under an N_2 atmosphere, a 10 mL dry round-bottom flask was charged with palladium acetylacetonate (6.1 mg, 0.02 mmol), ligand tri-tert-butylphosphonium tetrafluoroborate (11.6 mg, 0.04 mmol), trimethylsilyl oxanorbornadiene (43.2 mg, 0.2 mmol), 2-Bromonaphthalene (41.4 mg, 0.2 mmol), sodium phenoxide (34.8 mg, 0.3 mmol) and 2 mL DMF. The mixture was stirred at room temperature for 5 min, and then heated to 120 °C in oil bath. After 24 h, the reaction was cooled to room temperature, and diluted with ethyl acetate. The solution was filtered and concentrated under vacuum. The product was purified by flash chromatography (1:20 ethyl acetate/hexane) to obtain compound and then dissolved in 1 mL of $CHCl_3$ and 2 mL of *iso*-propanol, and the solution was transferred into microwave tube with a rubber septum and a stir bar. The solution was flushed with argon for 3 times, then 0.1 mL concentrated HCl was added. The tube was covered by alumina foil and taken into oil bath at 80 °C. After 12 h, the reaction was cooled down and 3 mL methanol was added. The solid was filter to get a light yellow solid. ^{1}H NMR ($CDCl_3$, 500 MHz,): δ 7.60 (dd, $J = 6.0$, 3.4 Hz, 4H), 7.33 (dd, $J = 6.1$, 3.3 Hz, 4H), 7.27 (s, 4H). The perchlorinated compounds ($C_{20}Cl_{12}$) as follows:

$C_{20}Cl_{12}$ was obtained by dissolving the aromatic hydrocarbon ($C_{20}H_{12}$) in the BMC reagent consisting of a mixture of S_2Cl_2 and $AlCl_3$ in a Cl equivalent ratio of 1:0.5 in 150 mL of SO_2Cl_2 and heating to 64 °C for 4 h. At the end of the reaction, the mixture was treated with icy water. After neutralization with $NaHCO_3$ the product was extracted with $CHCl_3$[45]. MS (MALDI-TOF): m/z calculated for $C_{20}Cl_{12}$:659.62; found: 659.50. ^{13}C NMR is not available because of extremely low solubility.

Density functional theory calculations and AFM simulations

Density functional theory (DFT) calculations were carried out in the gas phase using Gaussian 16 program package[46]. ωB97XD exchange-correlation functional[47] in conjunction with def2-TZVP[48] basis sets was used for C_{12} and C_{20} related calculations in gas phase.

The AFM simulations were conducted by the PP-AFM code provided by Hapala et al.[28]. The detailed parameters were listed below. The lateral spring constant for CO-tip was 0.2 N/m, and a quadrupole-like charge distribution at the tip apex was used to simulate the CO tip with $q = -0.1 e$. In addition, e is the elementary charge and refers to $|e|$, and q is the magnitude of quadrupole charge at the tip apex. The amplitude was set as 1 Å.

The Vienna ab initio simulation package (VASP)[49,50] was used to perform the DFT calculations on the NaCl surface. For describing the interaction between electrons and ions, the projector-augmented wave method[51,52] was used, and the Perdew−Burke−Ernzerhof generalized gradient approximation exchange−correlation functional was employed[53]. Van der Waals corrections were also included using the DFT-D3 method of Grimme[54]. The kinetic energy cutoff was set to 400 eV. We used a bilayer NaCl(001) slab separated by a vacuum thicker than 20 Å and the bottom layer of the NaCl was fixed. The atomic structures were relaxed until the atomic forces were less than 0.03 eV/ Å.

Data availability

References

1. Parent, D. C. & McElvany, S. W. Investigations of small carbon cluster-ion structures by reactions with hydrogen cyanide. *J. Am. Chem. Soc.* **111**, 2393–2401 (1989).
2. Van Orden, A. & Saykally, R. J. Small carbon clusters: spectroscopy, structure, and energetics. *Chem. Rev.* **98**, 2313–2357 (1998).
3. Grutter, M. et al. Electronic absorption spectra of linear C_6, C_8 and cyclic C_{10}, C_{12} in neon matrices. *J. Chem. Phys.* **111**, 7397–7401 (1999).
4. Diederich, F. Carbon scaffolding: building acetylenic all-carbon and carbon-rich compounds. *Nature* **369**, 199–207 (1994).
5. Pitzer, K. S. & Clementi, E. Large molecules in carbon vapor. *J. Am. Chem. Soc.* **81**, 4477–4485 (1959).
6. Parasuk, V., Almlof, J. & Feyereisen, M. W. The [18] all-carbon molecule: cumulene or polyacetylene? *J. Am. Chem. Soc.* **113**, 1049–1050 (1991).
7. Torelli, T. & Mitas, L. Electron correlation in C_{4N+2} carbon rings: aromatic versus dimerized structures. *Phys. Rev. Lett.* **85**, 1702–1705 (2000).
8. Arulmozhiraja, S. & Ohno, T. CCSD calculations on C_{14}, C_{18}, and C_{22} carbon clusters. *J. Chem. Phys.* **128**, 114301 (2008).
9. Remya, K. & Suresh, C. H. Carbon rings: a DFT study on geometry, aromaticity, intermolecular carbon–carbon interactions and stability. *RSC Advances* **6**, 44261–44271 (2016).
10. Baryshnikov, G. V., Valiev, R. R., Kuklin, A. V., Sundholm, D. & Agren, H. Cyclo[18]carbon: insight into electronic structure, aromaticity, and surface coupling. *J. Phys. Chem. Lett.* **10**, 6701–6705 (2019).
11. Baryshnikov, G. V. et al. Aromaticity of even-number cyclo[*n*]carbons (*n* = 6-100). *J. Phys. Chem. A* **124**, 10849–10855 (2020).
12. Charistos, N. D. & Muñoz-Castro, A. Induced magnetic field in sp-hybridized carbon rings: analysis of double aromaticity and anti-aromaticity in cyclo[2*N*]carbon allotropes. *Phys. Chem. Chem. Phys.* **22**, 9240–9249 (2020).
13. Baryshnikov, G. V. et al. Odd-number cyclo[*n*]carbons sustaining alternating aromaticity. *J. Phys. Chem. A* **126**, 2445–2452 (2022).
14. Brémond, E., Pérez-Jiménez, A. J., Adamo, C. & Sancho-García, J. C. Stability of the polyynic form of C_{18}, C_{22}, C_{26}, and C_{30} nanorings: a challenge tackled by range-separated double-hybrid density functionals. *Phys. Chem. Chem. Phys.* **24**, 4515–4525 (2022).

15. Li, M. et al. Potential molecular semiconductor devices: cyclo-C_n (n = 10 and 14) with higher stabilities and aromaticities than acknowledged cyclo-C_{18}. *Phys. Chem. Chem. Phys.* **22**, 4823–4831 (2020).

16. Kaiser, K. et al. An sp-hybridized molecular carbon allotrope, cyclo[18]carbon. *Science* **365**, 1299–1301 (2019).

17. Scriven, L. M. et al. Synthesis of cyclo[18]carbon via debromination of $C_{18}Br_6$. *J. Am. Chem. Soc.* **142**, 12921–12924 (2020).

18. Gao, Y. et al. On-surface synthesis of a doubly anti-aromatic carbon allotrope. *Nature* **623**, 977–981 (2023).

19. Sun, L. et al. On-surface synthesis of aromatic cyclo[10]carbon and cyclo[14]carbon. *Nature* **623**, 972–976 (2023).

20. von Helden, G., Hsu, M.-T., Kemper, P. R. & Bowers, M. T. Structures of carbon cluster ions from 3 to 60 atoms: Linears to rings to fullerenes. *J. Chem. Phys.* **95**, 3835–3837 (1991).

21. von Helden, G., Gotts, N. G. & Bowers, M. T. Experimental evidence for the formation of fullerenes by collisional heating of carbon rings in the gas phase. *Nature* **363**, 60–63 (1993).

22. Anderson, H. L., Patrick, C. W., Scriven, L. M. & Woltering, S. L. A short history of cyclocarbons. *Bull. Chem. Soc. Jpn.* **94**, 798–811 (2021).

23. Jones, R. O. Density functional study of carbon clusters C_{2n} ($2 \leqslant n \leqslant 16$). I. Structure and bonding in the neutral clusters. *J. Chem. Phys.* **110**, 5189–5200 (1999).

24. Manna, D. & Martin, J. M. What are the ground state structures of C_{20} and C_{24}? An explicitly correlated Ab Initio approach. *J. Phys. Chem. A* **120**, 153–160 (2016).

25. Feyereisen, M., Gutowski, M., Simons, J. & Almlöf, J. Relative stabilities of fullerene, cumulene, and polyacetylene structures for C_n: n=18–60. *J. Chem. Phys.* **96**, 2926–2932 (1992).

26. Prinzbach, H. et al. Gas-phase production and photoelectron spectroscopy of the smallest fullerene, C_{20}. *Nature* **407**, 60–63 (2000).

27. Albrecht, F. et al. The odd-number cyclo[13]carbon and its dimer, cyclo[26]carbon. *Science* **384**, 677–682 (2024).

28. Hapala, P. et al. Mechanism of high-resolution STM/AFM imaging with functionalized tips. *Phys. Rev. B* **90**, 085421 (2014).

29. Dobrowolski, M. A., Cyranski, M. K. & Wrobel, Z. Cyclic π-electron delocalization in non-planar linear acenes. *Phys. Chem. Chem. Phys.* **18**, 11813–11820 (2016).

30. Liu, M. et al. Thermally induced transformation of nonhexagonal carbon rings in graphene-like nanoribbons. *J. Phys. Chem. C* **122**, 9586–9592 (2018).

31. Preda, D. V. & Scott, L. T. Phenyl migrations in dehydroaromatic compounds. A new mechanistic link between alternant and non-alternant hydrocarbons at high temperatures. *Org. Lett.* **2**, 1489–1492 (2000).

32. Jones, R. R. & Bergman, R. G. *p*-Benzyne. Generation as an intermediate in a thermal isomerization reaction and trapping evidence for the 1,4-benzenediyl structure. *J. Am. Chem. Soc.* **94**, 660–661 (1972).

33. Schuler, B. et al. Reversible Bergman cyclization by atomic manipulation. *Nat. Chem.* **8**, 220–224 (2016).

34. Albrecht, F. et al. Selectivity in single-molecule reactions by tip-induced redox chemistry. *Science* **377**, 298–301 (2022).

35. Wong, H. N. C., Garratt, P. J. & Sondheimer, F. Unsaturated eight-membered ring compounds. XI. Synthesis of sym-dibenzo-1,5-cyclooctadiene-3,7-diyne and sym-dibenzo-1,3,5-cyclooctatrien-7-yne, presumably planar conjugated eight-membered ring compounds. *J. Am. Chem. Soc.* **96**, 5604–5605 (1974).

36. Kawai, S. et al. An endergonic synthesis of single Sondheimer-Wong diyne by local probe chemistry. *Angew. Chem. Int. Ed.* **59**, 10842–10847 (2020).

37. Suresh, R. et al. Cyclo[18]carbon formation from $C_{18}Br_6$ and $C_{18}(CO)_6$ precursors. *J. Phys. Chem. Lett.* **13**, 10318–10325 (2022).

38. Pavliček, N. et al. Polyyne formation via skeletal rearrangement induced by atomic manipulation. *Nat. Chem.* **10**, 853–858 (2018).

39. Repp, J., Meyer, G., Stojković, S. M., Gourdon, A. & Joachim, C. Molecules on insulating films: Scanning-tunneling microscopy imaging of individual molecular orbitals. *Phys. Rev. Lett.* **94**, 026803 (2005).

40. Schlutter, F., Nishiuchi, T., Enkelmann, V. & Mullen, K. Octa-functionalized biphenylenes: molecular precursors for isomeric graphene nanostructures. *Angew. Chem. Int. Ed.* **53**, 1538–1542 (2014).

41. Gross, L., Mohn, F., Moll, N., Liljeroth, P. & Meyer, G. The chemical structure of a molecule resolved by atomic force microscopy. *Science* **325**, 1110–1114 (2009).

42. Giessibl, F. J. High-speed force sensor for force microscopy and profilometry utilizing a quartz tuning fork. *Appl. Phys. Lett.* **73**, 3956–3958 (1998).

43. Albrecht, T. R., Grütter, P., Horne, D. & Rugar, D. Frequency modulation detection using high-Q cantilevers for enhanced force microscope sensitivity. *J. Appl. Phys.* **69**, 668–673 (1991).

44. Yin, X., Zheng, K., Jin, Z., Horst, M. & Xia, Y. Synthesis of contorted polycyclic conjugated hydrocarbons via regioselective activation of cyclobutadienoids. *J. Am. Chem. Soc.* **144**, 12715–12724 (2022).

45. Sun, J., Grutzmacher, H. F. & Lifshitz, C. Ion/molecule reactions of carbon cluster ions and acrylonitrile. *J. Am. Chem. Soc.* **115**, 8382–8388 (1993).

46. Frisch, M. J. et al. Gaussian 16 Rev. C.01; Gaussian, Inc.:Wallingford, CT. (2016).

47. Chai, J. D. & Head-Gordon, M. Long-range corrected hybrid density functionals with damped atom-atom dispersion corrections. *Phys. Chem. Chem. Phys.* **10**, 6615–6620 (2008).

48. Weigend, F. & Ahlrichs, R. Balanced basis sets of split valence, triple zeta valence and quadruple zeta valence quality for H to Rn: Design and assessment of accuracy. *Phys. Chem. Chem. Phys.* **7**, 3297–3305 (2005).

49. Kresse, G. & Hafner, J. Ab initio molecular dynamics for open-shell transition metals. *Phys. Rev. B* **48**, 13115–13118 (1993).

50. Kresse, G. & Furthmüller, J. Efficient iterative schemes for ab initio total-energy calculations using a plane-wave basis set. *Phys. Rev. B* **54**, 11169–11186 (1996).

51. Blöchl, P. E. Projector augmented-wave method. *Phys. Rev. B* **50**, 17953–17979 (1994).

52. Kresse, G. & Joubert, D. From ultrasoft pseudopotentials to the projector augmented-wave method. *Phys. Rev. B* **59**, 1758–1775 (1999).

53. Perdew, J. P., Burke, K. & Ernzerhof, M. Generalized gradient approximation made simple. *Phys. Rev. Lett.* **77**, 3865–3868 (1996).

54. Grimme, S., Antony, J., Ehrlich, S. & Krieg, H. A consistent and accurate ab initio parametrization of density functional dispersion correction (DFT-D) for the 94 elements H-Pu. *J. Chem. Phys.* **132**, 154104 (2010).

Acknowledgements

Author contributions

W.X. conceived the research; L.S., F.K., and W.G. performed the STM/AFM experiments; L.S., T.W. and G.G. carried out the DFT calculations; W.Z. synthesized the $C_{12}Br_4I_4$ and $C_{20}Cl_{12}$ precursors; all authors contributed to writing the manuscript. L.S. and W.Z. contributed equally to this work.

Competing interests

The authors declare no competing interests.

Additional information

Publisher's note Springer Nature remains neutral with regard to jurisdictional claims in published maps and institutional affiliations.